Original Article

Estimation of Proton Stopping Power Ratio and Mean Excitation Energy Using Electron Density and Its Applications via Machine Learning Approach

Charles Ekene Chika
Department of Mathematics, University of Nigeria, Nsukka, Enugu, Nigeria

Abstract

Purpose: The purpose of this study was to develop a simple flexible method for accurate estimation of stopping power ratio (SPR) and mean excitation energy (I) using relative electron density (ρ_e). **Materials and Methods:** The model was formulated using empirical relationships between SPR, mean excitation energy I, and relative electron density. Some examples were implemented, and a comparison was carried out using other existing methods. The needed coefficients in the model were estimated using optimization tools. Basis vector method (BVM) and Hunemohr and Saito (H-S) method were applied to estimate the ρ_e used in the application section. 80 kVp and 150 kVpSn were used as low and high energy, respectively, for the implementation of dual-energy methods. **Results:** All the examples of the proposed method considered have modeling error that is ≤0.32% and testing root mean square error (RMSE) ≤0.92% for SPR with a mean error close to 0.00%. The method was able to achieve modeling RMSE of 2.12% for mean excitation energy with room for improvement. Similar or better results were achieved in application to BVM. **Conclusion:** The method showed robustness in application by achieving lower testing error than other presented methods in most cases. It achieved accurate estimation which can be improved using the machine learning algorithm since it is flexible to implement in terms of the function (model) degree and tissue classification.

Keywords: Computed tomography image, machine learning, mathematical model, optimization, proton stopping power ratio, proton therapy, tumor treatment

Received on: 16-11-2023 **Review completed on:** 18-03-2024 **Accepted on:** 24-04-2024 **Published on:** 25-06-2024

Introduction

Proton stopping power ratio (SPR) is used to compute proton range for proton therapy treatment. This helps utilize the property of proton known as Bragg peak, which gives it advantage over photon during therapy. The necessity to improve proton therapy treatment leads to finding ways of estimating SPR more accurately, which also depends on relative electron density (ρ_e) and mean excitation energy (I) through Bethe equation or Bethe–Bloch equation.[1-8]

There are mainly two ways of estimating ρ_e, I and SPR in terms of domain; these are image and projection domain approach. Image domain uses computed tomography (CT) image to estimate these quantities and has the advantage of simplicity in computation compared to projection domain but has the disadvantage of being prone to uncertainties such as noise, movements, and beam hardening. The projection domain has the advantage of being less prone to uncertainties as some causes of uncertainties such as beam hardening can be corrected on the projection data, but it has the disadvantage of being computational intensive. Many authors have presented studies on image domain[8-43] and many on projection domain[4,5,32-38,44-51] including the analysis of their uncertainties.[52] There are some approaches that might help improve projection domain calculation but still under development like the one by Chika and Hooshyar.[2]

Another approach is based on the number of energy spectra used. The most popularly known clinically used method is single-energy CT stoichiometric calibration method which is

Address for correspondence: Dr. Charles Ekene Chika, Department of Mathematics, University of Nigeria, Nsukka, Enugu, Nigeria.
E-mail: charles.chika@unn.edu.ng

Access this article online

Quick Response Code:

Website: www.jmp.org.in

DOI: 10.4103/jmp.jmp_157_23

How to cite this article: Chika CE. Estimation of proton stopping power ratio and mean excitation energy using electron density and its applications via machine learning approach. J Med Phys 2024;49:155-66.

image domain method. 3%–3.5% of proton range is being added to the distal boundary of clinical target volume when using this method for patients' safety.[5,53] Dual-energy CT (DECT) approach is another one that is currently being explored much. This makes use of two energy spectra referred to as low- and high-energy spectra. DECT has better performance as regards to uncertainties as demonstrated in the study by Yang *et al*.[8] and other studies. Chenyang Shen *et al*.[6] and other authors have proposed multi-energy approach as well.

Most of the approaches being proposed are targeted at estimating SPR directly or estimating ρ_e and I and then applying it to Bethe equation or Bethe–Bloch equation to estimate stopping power (SP) or SPR. Some of these methods, especially those of projection domain, have a high accuracy in estimating relative electron density ρe (with root mean square error [RMSE] of <1%) but have relatively low accuracy in estimating effective atomic number (with RMSE of more than 3%) which is used to estimate mean excitation energy mainly using Yang method.[7,54,55] This called for accurate means of estimating SPR using ρ_e to reduce the error propagation which led to this study.

In this study, we present a model that estimates SPR and I from ρ_e, discussed its accuracy and applications. Two dual energy and image domain methods which are referred to as Hunemorh and Saito (H-S) method and basis vector method (BVM) were used to estimate the re in the application section. This method is compared to some other methods that have been proposed. Algorithm is also presented that will help in automation.

Materials and Methods

Data acquisition

Computed tomography data

Linear attenuation and the image intensity HU_k of each pixel/voxel in CT images for any tissue are written as:

$$<\frac{\mu}{\mu_{wat}}>_k=\frac{HU_k}{A_k}+A_k^* \quad (1)$$

where μ_{wat} is the linear attenuation coefficient of water and μ is that of unknown tissue. Low- and high-energy spectra were represented by the subscript k = L, H. The parameters A_k and A_k^* are calculated by maximizing the fit between measured HU_K and spectrally averaged.

$<\frac{\mu}{\mu_{wat}}>_k$ values for scanned sampled tissues of known composition and density.

We assumed that a phantom consisting of unknown tissues is scanned with the commercial CT scanner at low-energy (k = L) and high-energy (k = H) spectra, characterized by normalized X-ray energy fluence spectra $\Psi_k(E)$ where $\int_E \Psi_k(E)dE = 1$.

$$<\frac{\mu}{\mu_{wat}}>_k=\frac{\int_E \Psi_k(E)\mu(x,E)dE}{\int_E \Psi_k(E)\mu_{wat}(x,E)dE}, \quad (2)$$

Commercial CT scanner spectra are generally not precisely known. HU measurements can be influenced by beam hardening, scattering, noise, and prepossessing corrections, which leads to uncertainties in the measurement. k (E) is approximated by a single effective energy E_K most of the times, so that $\frac{\mu_s(E_k)}{\mu_{wat}(E_k)}=<\frac{\mu_s(E)}{\mu_{wat}(E)}>_k=\mu_{ef,s}$. This $\mu_{ef,s}$ is gotten by minimizing the difference between the theoretical CT numbers computed from Eq(2) and that of single energies, μ(x,E). Mixture rule is used to compute the linear attenuation coefficients. It is computed by applying the mixture rule to elemental mass attenuation coefficients gotten from the National Institute of Standards and Technology XCOM database using tissue composition.[56-60] Once this is done, Eq. (2) is applied. Figure 1 illustrates the normalized form of the spectra used for computation in Eq (2) which is generated using SpekCalc.[61,62] 80 kVp and 150 kVp are used as low and high energy, respectively.

Relative electron density (ρ_e)

True relative electron density is computed using the following formula:

$$\rho_e=\frac{\rho_{e,x}}{\rho_{e,w}}=\frac{\rho_x\sum_{i=1}^{M}\frac{\omega_i Z_i}{A_i}}{\rho_{e,w}} \quad (3)$$

where $\rho_{e,x}$ denotes the mass density. ω_i, Z_i, and A_i are the mass fraction, atomic number, and atomic mass of the i^{th} element in the tissue, respectively.

Mean excitation energy I

Bragg additivity rule was applied in computing the true mean excitation energy for each tissue:

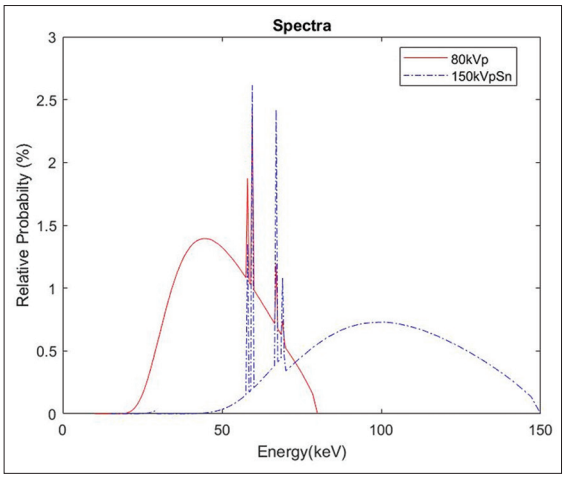

Figure 1: Spectra used (80 kVp and 150 kVpSn normalized spectra used to compute theoretical attenuation coefficients)

$$\ln(I) = \frac{\sum_i \omega_i \left(\frac{Z}{A}\right)_i \ln(I_i)}{\sum_i \omega_i \left(\frac{Z}{A}\right)_i} \quad (4)$$

I_i is the mean excitation energy of the i^{th} element in the tissue.

Stopping power ratio

The simplified form of Bethe equation referred to as Bethe–Bloch equation is used to compute the true *SPR* . The equation is stated below:

$$SPR = \rho_e \frac{\ln\frac{2m_e c^2\beta^2}{1-\beta^2} - \beta^2 - \ln I}{\ln\frac{2m_e c^2\beta^2}{1-\beta^2} - \beta^2 - \ln I_w} \quad (5)$$

where m_e is the rest mass of an electron, c is the speed of light, β is the velocity of the proton in vacuum relative to the speed of light, and I_W is the mean excitation energy of water. This is used to approximate the SP at a given energy E within the range typically used in proton therapy.

Tissue classification

Thirty-three ICRU [Appendix] human tissues[63-65] are used as training data and 12 Gammex tissue inserts as validation data. Nucleus was not included in ICRU human tissues because we cannot access its composition at the time of the study.

The human tissues are classified into lung, soft, and bone tissues, while the Gammex inserts are classified into soft and bone tissues. All the classifications in this study are done with the ρ_e. The regions illustrated in Figure 2 represent the grouping.

Proposed model

Proposition: SPR and mean excitation energy are empirically related to electron density by the relation:

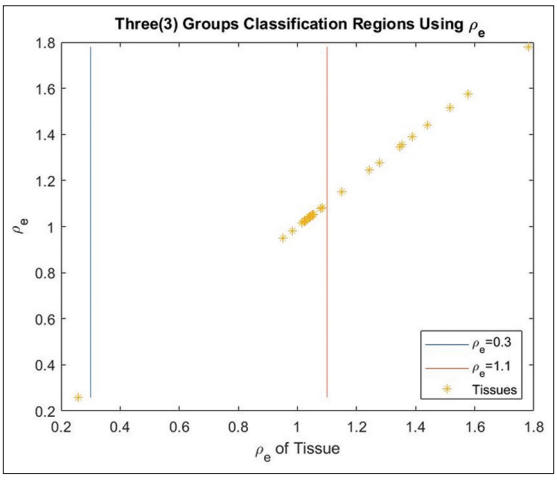

Figure 2: This figure illustrates the regions of the three tissues: The first region from the left is for lung tissues, the middle is for soft tissues and the right-most region is for bone tissues

$$T(SPR/I) = \sum_{i=-r}^{n} a_i \rho_e^i + error \quad (6)$$

where $n \geq 0$, $r \geq 0$, and T (SPR/*I*) is an invertible transformation of SPR or *I*.

For this first study, the model examples are proposed using the graphical exploration of the data relationships and the knowledge of mathematical functions.

Stopping power ratio

The model below was implemented for SPR:

$$SPR = \sum_{i=-r}^{n} a_i \rho_e^i + error \quad (7)$$

where $n \geq 0$, $r \geq 0$ and T (SPR) = SPR. We will follow the notation $SPR_{r,n}$ and present simple continuous and piece-wise functions. The following three models were studied.

Continuous models

$$SPR_{0,3} = 0.0574\rho_e^3 - 0.2564\rho_e^2 + 1.2551\rho_e - 0.0493 \quad (8)$$

$$SPR_{1,1} = 0.862\rho_e + 0.1822 - \frac{0.0373}{\rho_e} \quad (9)$$

Piece-wise model

$$SPR_{1,1} = \begin{cases} 0.2578, & lungtissue \\ 1.6008\rho_e - 1.3931 + \frac{0.8012}{\rho_e}, & softtissue \\ 0.8612\rho_e + 0.1791 - \frac{0.0301}{\rho_e}, & bonetissue \end{cases} \quad (10)$$

Kanematsu method

We compared the proposed model with the one proposed by Kanematsu *et al*.[66] A poly-line relation between $\frac{SPR}{\rho_e}$ and ρ_e is presented below:

$$\frac{SPR}{\rho_e} = \begin{cases} 1.0002, & lungtissue \\ -0.2936\rho_e^2 + 1.0039\rho_e + 0.3135, & softtissue \\ -0.0038\rho_e^2 + 0.2568\rho_e + 0.7462, & bonetissue \end{cases} \quad (11)$$

Mean excitation energy I

We used the model stated below for illustration in the case of mean excitation energy.

$$\ln(I) = \sum_{i=-r}^{n} a_i \rho_e^i + error \quad (12)$$

where $n \geq 0$, $r \geq 0$, preferably $n = 2k$, $k \geq 0$, and $T(I) = ln(I)$

Just as in above, we follow the notation $I_{r,n}$ and present two examples.

Continuous models

$$\ln(I_{1,2}) = -0.4782\rho_e^2 + 2.1353\rho_e + 2.1970 + \frac{0.4109}{\rho_e} \quad (13)$$

Piece-wise model

$$\ln(I_{1,0}) = \begin{cases} 4.3197, & lungtissue \\ 5.4233 + \dfrac{-1.171}{\rho_e}, & softtissue \\ 5.3630 - \dfrac{-1.151}{\rho_e}, & bonetissue \end{cases} \quad (14)$$

Application

Basis vector method

We implemented the proposed model above and compared it to the values gotten from BVM. In this study, we used 23% aqueous calcium chloride ($cacl_2$) solution and polystyrene as dissimilar basis materials. Other materials such as water and aluminum can be used, with the water representing soft tissue and aluminum representing bone tissue. Some studies apply different materials to different tissue groups like the one by Han *et al*.[28] The basis vector model for dual energy is presented below:

$$\mu_l = c_1(x)\mu_{1,l} + c_2(x)\mu_{2,l} \quad (15)$$

where μ_i is the unknown tissue linear attenuation at high and low energies, $\mu_{j,l}$ represents the basis material linear attenuation coefficient at high and low energies, and c_j is the energy-independent weight $j = 1,2$ and $l = L,H$. The energy-independent weights can be calculated as below:

$$\begin{bmatrix} c_1(x) \\ c_2(x) \end{bmatrix} = \begin{bmatrix} \mu_{1,L} & \mu_{2,L} \\ \mu_{1,H} & \mu_{2,H} \end{bmatrix}^{-1} \begin{bmatrix} \mu_L \\ \mu_H \end{bmatrix} \quad (16)$$

After calculating the weight, relative electron density of the unknown material is calculated using the relation below:

$$\rho_e = c_1\rho_{e,1} + c_2\rho_{e,2} \quad (17)$$

where $\rho_{e,l}$ and $\rho_{e,2}$ are the basis materials' relative electron density. We implemented the two approaches that have been used to compute the mean excitation energy by Han *et al*.[28] and Shuangyue *et al*.[4]

$$I_{fc} = f\left(\frac{c_1}{c_1 + c_2}\right) exp\left(\frac{c_1\rho_{e,1}\ln I_1 + c_2\rho_{e,2}\ln I_2}{c_1\rho_{e,1} + c_2\rho_{e,2}}\right) \quad (18)$$

$$I_{rc} = exp(a_1 r_c(x) + a_0) \quad (19)$$

where,

$$r_c(x) = \frac{c_1(x)\rho_{e,1}}{c_1(x)\rho_{e,1} + c_2(x)\rho_{e,2}}$$

$$f\left(\frac{c_1}{c_1 + c_2}\right) = a_1\frac{c_1}{c_1 + c_2} + a_0$$

a and b are constants to be determined through calibration from the given mean excitation energy and $f\left(\frac{c_1}{c_1 + c_2}\right)$ is referred to as an empirical correction function of $\rho_e I_{fc} = c_1\rho_{e,1}\ln I_1 + c_2\rho_{e,2}\ln I_2$. Once ρ_e and I are known, *SPR* is computed using Bethe–Bloch equation.

$$f(c_1, c_2) = \begin{cases} 1.7767, & lungtissue \\ 0.5290c_r + 1.6902, & softtissue \\ -0.5651c_r + 1.5859, & bonetissue \end{cases} \quad (20)$$

$$\ln(I_{r_c}) = \begin{cases} 4.3197, & lungtissue \\ 1.0752r_c + 4.1504, & softtissue \\ 0.3424r_c + 4.1815, & bonetissue \end{cases} \quad (21)$$

$$SPR_{1,1} = \begin{cases} 0.2579, & lungtissue \\ 1.7458\rho_e^2 - 1.6986\rho_e + \dfrac{0.9609}{\rho_e}, & softtissue \\ 0.8618\rho_e^2 + 0.1778\rho_e - \dfrac{0.0292}{\rho_e}, & bonetissue \end{cases} \quad (22)$$

$$\ln(I_{1,0}) = \begin{cases} 4.3197, & lungtissue \\ 5.7569 - \dfrac{1.5160}{\rho_e}, & softtissue \\ 5.3642 - \dfrac{1.1526}{\rho_e}, & bonetissue \end{cases} \quad (23)$$

Hunemohr–Saito method (H-S)

Hunemohr–Saito method is the method developed by Hunemohr *et al*.[14] whose similar ρ_e formula has been previously presented by Saito. We applied the method to the relative electron density computed by Hunemohr–Saito method and compared it with the usual computed I and SPR. The H-S model is presented below:

$$\frac{\rho_e}{\rho_{e,w}} = a\mu_1 + (1-a)\mu_2 \quad (24)$$

$$Z_{ef} = \left(\left(\frac{\rho_e}{\rho_{e,w}}\right)^{-1}(b\mu_1 + (Z_{e,w}^n - b)\mu_2)\right)^{\frac{1}{n}} \quad (25)$$

The model parameters, a and b, depend on specific dual-energy scanning protocol. SPR is estimated from the values of ρ_e and Z_{ef} images using the empirical relationship between I-value and Z_{ef} which was first introduced by Yang *et al*.[7] The empirical relationship is as follows.

$$\ln(I)=\begin{cases}a_l, & \mu_L \le 0.3\\ a_s Z_{ef}+b_s, & \mu_L \le 1.4\\ a_b Z_{ef}+b_b, & \mu_L > 1.4\end{cases} \quad (26)$$

$$\ln(I_{1,0})=\begin{cases}4.3197, & lungtissue\\ 5.7632-\dfrac{1.5204}{\rho_e}, & softtissue\\ 5.3617-\dfrac{1.1489}{\rho_e}, & bonetissue\end{cases} \quad (27)$$

$$SPR_{1,1}=\begin{cases}0.2579, & lungtissue\\ 1.7477\rho_e^2-1.6925\rho_e+\dfrac{0.9538}{\rho_e}, & softtissue\\ 0.8586\rho_e^2+0.1832\rho_e-\dfrac{-0.0303}{\rho_e}, & bonetissue\end{cases} \quad (28)$$

Accuracy analysis

$$ME=\frac{1}{N}\sum_{i=1}^{N} error_i \quad (29)$$

$$RMSE=\sqrt{\frac{\sum_{i=1}^{N} error_i^2}{N}} \quad (30)$$

where relative error is defined as

$$error=\frac{SPR_{true}-SPR_{est}}{SPR_{true}} \quad (31)$$

or

$$error=\frac{I_{true}-I_{est}}{I_{true}} \quad (32)$$

I_{true} is the reference I value and I_{est} is the estimated I value, the same definition holds for SPR. The mean error (ME) measures the bias of the value estimates and RMSE measures the estimation error for different tissues.

Results

Stopping power ratio

SPR1,1 piece-wise gave the best result in training with training RMSE of 0.22% and ME of 0.00%, while SPR0,3 continuous gives the least testing RMSE of and the least testing ME is given by SPR1,1 piece-wise which is 0.04%. Kinematsu method gave the highest error among all the methods presented for SPR both in training and testing data; it gives training RMSE of 2.03%, testing RMSE of 1.77%, training ME of −1.85%, and testing ME of −1.61%. These information are shown in Tables 1 and 2. From Figures 3 and 4, Kinematsu method gave mainly underestimated values and the error increases with an increase in SPR value for bone tissues.

Mean excitation energy *I*

Tables 3 and 4 show that $I_{1,0}$ performs better in training data with RMSE of 1.12%, while $I_{1,2}$ performs better in testing. $I_{1,0}$ is less biased in testing data and more biased on training data compared to $I_{1,2}$ since it has training and testing MEs of 0.11% and −1.58%, respectively, while that of $I_{1,2}$ are −0.02% and −2.51%.

Application results

The use of linear attenuation coefficients at effective energy to estimate relative electron density (ρ_e) shows that H-S method performs better on training data with total RMSE of 0.04% and ME of 0.02%, while BVM performs better on testing data

Table 1: Stopping power ratio training and testing root mean square errors (%)

SPR training RMSE	Total	Lung	Soft	Bone	Testing RMSE	Total	Soft	Bone
$SPR_{1,1}$ continuous	0.32	0.70	0.35	0.13		0.73	0.80	0.62
$SPR_{1,1}$ piece-wise	0.22	0.02	0.27	0.04		0.92	1.09	0.61
$SPR_{0,3}$ continuous	0.31	0.14	0.38	0.07		0.71	0.77	0.62
Kinematsu	2.03	0.00	2.08	2.04		1.77	1.80	1.63

RMSE: Root mean square error, SPR: Stopping power ratio

Table 2: Stopping power ratio training and testing mean errors (%)

SPR training ME	Total	Lung	Soft	Bone	Testing RMSE	Total	Soft	Bone
$SPR_{1,1}$ continuous	0.02	0.73	0.01	0.09		0.29	0.32	0.24
$SPR_{1,1}$ piece-wise	0.00	0.02	0.00	0.01		0.04	−0.05	0.17
$SPR_{0,3}$ continuous	0.00	0.14	−0.02	0.04		0.28	0.34	0.19
Kinematsu	−1.85	0.00	−1.95	−1.83		−1.61	−1.76	−1.28

ME: Mean error, RMSE: Root mean square error, SPR: Stopping power ratio

with total RMSE of 0.05% and ME of 0.01%, as can be seen in Table 5. Figure 5 shows that BVM achieved less testing error for most soft tissues compared to training error, while H-S does the opposite. Though, all errors are quite low.

Stopping power ratio

From Table 6, $SPR_{1,1}$ gave the best training error among the ones presented when applied to both the re estimated using BVM and H-S method. The total RMSE for both applied cases is 0.23% and 0.22%, respectively. SPR from $I_{1,0}$ gave the least testing RMSE of 0.86% in BVM and RMSE of 0.85% for H-S method while $SPR_{1,1}$ gave the least RMSE for bone in both BVM and H-S method which are 0.61% and 0.63%, respectively. $SPR_{1,1}$ gave the least bias estimation in both BVM and H-S method with ME of 0.00%. In BVM, all the total RMSE (both modeling and testing) are <1% except that estimated from I_{fc} and I_{rc}. This can be seen in Table 7. Figures 6 and 7 show that the approaches presented achieved relatively low training errors for each tissue while Figure 8 shows a relatively higher error for inner bone (Gammex insert) for the case of I_{fc} and I_{rc} while all others remains relatively low. Figure 9 shows that the method still achieved low testing errors for each tissue in H-S method.

Mean excitation energy *I*

Table 8 shows that $I_{1,0}$ has the least training RMSE in BVM for bone tissues which is 0.27%, it also has same for H-S method and total least RMSE of 1.94%. Although I_{rc} has the lowest training error of 1.85% for BVM, it has a very high total RMSE of 15.15% and 22.68 for bone. $I_{1,0}$ has the least testing error for BVM with a value of 7.19%. All the estimations of I using BVM achieved the same level of biasedness with ME of −0.01% on training data while $I_{1,0}$ achieved the least ME for both BVM and H-S method which are −1.08% and −1.09% on testing data, and it has the least training ME for H-S method as well which is −0.02%, as can be seen in Table 9. Figure 10 shows that $I_{1,0}$ performs better in bone tissues while the performance of all the presented methods is similar in most of the soft tissues in training data. Inner bone has an off-high testing error on I_{fc} and I_{rc}, as can be seen in Figure 11.

Discussion

The method presented estimates SPR with high accuracy, as can be seen from Figures 12-14 and Tables 1 and 2 on training and testing errors. Figures 12 and 13 show that we do not need to group the tissues to get good estimates of SPR. Increasing the fitting degrees can improve the accuracy but we have to be conscious of overfitting. Grouping the tissues also improves the accuracy. The method presented performs better than Kinematsu method which is the study we found on estimating SPR using ρ_e. The absolute relative error for Kinematsu method is increasing with ρ_e which suggests that some corrections might be possible. $SPR_{1,1}$ gave the least modeling error though not the least testing error, but we chose it for application because current studies normally divide the tissues into

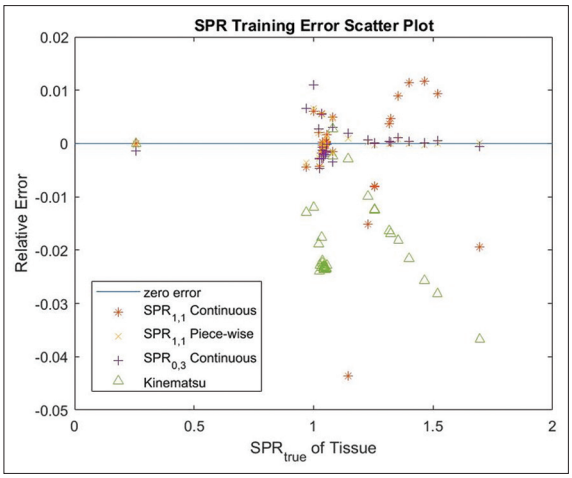

Figure 3: Stopping power ratio training errors for individual tissues used for model training. SPR: Stopping power ratio

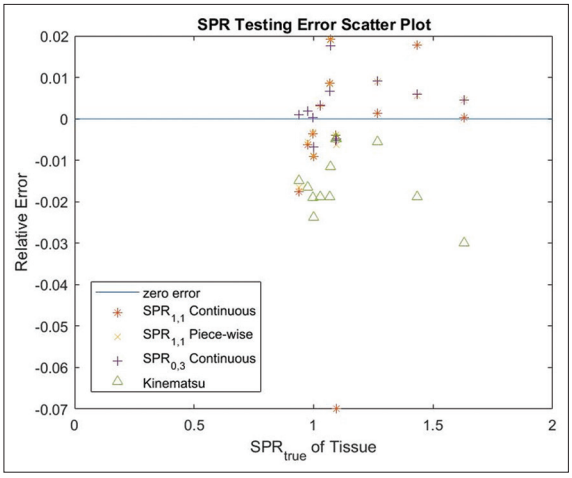

Figure 4: Stopping power ratio testing errors for individual tissues used for testing. SPR: Stopping power ratio

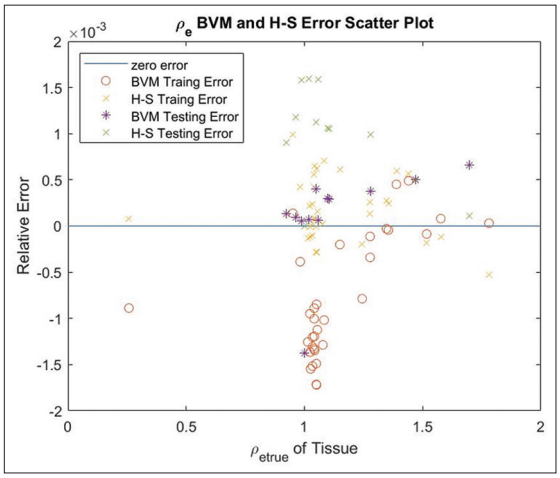

Figure 5: ρ_e training and testing errors for individual tissues used (this is for both H-S and basis vector method methods as presented in the figure, it's comparing true relative electron density with the relative electron density estimated by these two methods). BVM: Basis vector method, H-S: Hunemohr and Saito

3 groups. On application, we see that the model performance was good on both BVM and H-S method. This performance may also be a result of these two methods predicting ρ_e with a high accuracy. This aligns with the aim of this study which is applying this method to projection domain methods which already have high accuracy estimation of ρ_e. $SPR_{r,n}$ will be a good option in terms of accuracy and computation time savings since the use of Bethe equation will be skipped.

Figures 15 and 16 show that the proposed model $I_{r,n}$ can give a good fit to ρ_e data whether the tissues are grouped or not.

Table 3: *I* training and testing root mean square errors (%)

I training RMSE	Total	Lung	Soft	Bone	Testing RMSE	Total	Soft	Bone
$I_{1,0}$	2.12	0.00	2.65	0.29		6.62	7.49	5.16
$I_{1,2}$	2.63	1.02	3.26	0.61		6.25	6.94	5.14

RMSE: Root mean square error

Table 4: *I* training and testing mean errors (%)

I Training ME	Total	Lung	Soft	Bone	Testing RMSE	Total	Soft	Bone
$I_{1,0}$	0.11	0.00	0.16	0.00		−1.58	−1.70	−1.41
$I_{1,2}$	−0.02	1.02	0.10	−0.35		−2.51	−3.13	−1.65

ME: Mean error, RMSE: Root mean square error

We plotted ρ_e ln(I) for easy visualization. $I_{r,n}$ gives a good result both in BVM and H-S method. I_{fc} and I_{rc} have high testing errors, especially for bone, and that makes them less robust. This might be due to difference in computed weights that follow from composition variation since Ifc and Irc depend on these weights. This may still be a similar reason why they have high relative error for inner bone. Estimating I using H-S method gives less testing error but this is not in line with the aim of this study since it computes I using Z, this does not translate into much difference when used to estimate SPR and it gives a higher ME (−3.14%) if compared with $I_{1,0}$ (which has ME of −1.09%), this indicates that it can be more biased. This also works well only when the tissues are grouped into lung, soft, and bone tissues.

This model can be generalized as:

$$T(SPR/I,\rho_e)=\sum_{i=-r}^{n}a_i\rho_e^i+error$$

where $n \geq 0$, $r \geq 0$ and T (SPR/I, ρ_e) is an invertible transformation of SPR or I and ρ_e.

Kinematsu method will belong to the class of model above since the one presented here can be written as:

$$T(SPR,\rho_e)=\frac{SPR}{\rho_e}=\sum_{i=0}^{2}a_i\rho_e^i+error$$

Table 5: ρ_e training and testing errors (%)

ρ_e training RMSE	Total	Lung	Soft	Bone	Testing RMSE	Total	Soft	Bone
BVM RMSE	0.10	0.09	0.12	0.03		0.05	0.05	0.04
H-S RMSE	0.04	0.01	0.04	0.04		0.11	0.13	0.08
BVM ME	−0.08	−0.09	−0.12	0.00		0.01	−0.01	0.04
H-S ME	0.02	0.01	0.02	0.02		0.10	0.11	0.07

ME: Mean error, RMSE: Root mean square error, BVM: Basis vector method, H-S: Hunemohr and Saito

Table 6: Stopping power ratio training and testing mean error (%)

SPR training ME	Total	Lung	Soft	Bone	Testing ME	Total	Soft	Bone
BVM SPR from $I_{1,0}$	−0.08	−0.14	−0.12	0.00		0.12	0.02	0.25
BVM $SPR_{1,1}$	0.00	0.07	0.00	−0.01		0.08	−0.01	0.22
BVM SPR from I_{fc}	−0.08	−0.09	−0.11	−0.01		0.75	0.37	1.28
BVM SPR from I_{rc}	−0.08	−0.09	−0.12	−0.01		0.79	0.36	1.39
H-S SPR from $I_{1,0}$	0.95	0.94	0.95	0.95		1.14	1.08	1.22

BVM: Basis vector method, H-S: Hunemohr and Saito, SPR: Stopping power ratio, ME: Mean error

Table 7: Stopping power ratio training and testing root mean square error (%)

SPR training RMSE	Total	Lung	Soft	Bone	Testing RMSE	Total	Soft	Bone
BVM SPR from $I_{1,0}$	0.26	0.14	0.32	0.06		0.86	0.99	0.63
BVM $SPR_{1,1}$	0.23	0.07	0.28	0.05		0.98	1.18	0.61
BVM SPR from I_{fc}	0.29	−0.09	0.31	0.28		1.59	0.61	2.36
BVM SPR from I_{rc}	0.25	0.09	0.30	0.13		1.54	0.61	2.27
H-S SPR from $I_{1,0}$	0.98	0.94	1.00	0.95		1.40	1.45	1.33
H-S $SPR_{1,1}$	0.22	0.01	0.27	0.05		0.97	1.15	0.63
H-S	0.39	0.28	0.41	0.35		0.85	0.91	0.77

RMSE: Root mean square error, BVM: Basis vector method, H-S: Hunemohr and Saito, SPR: Stopping power ratio

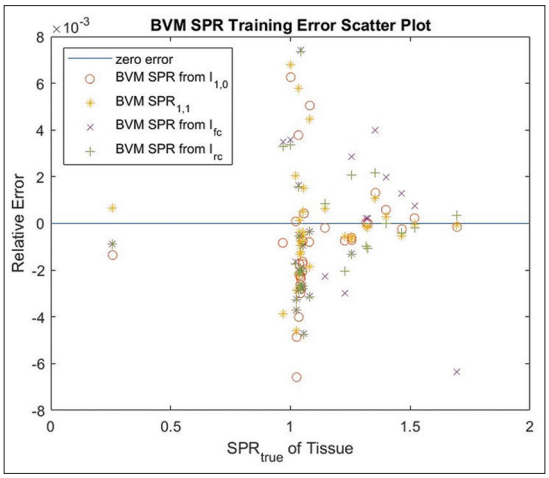

Figure 6: Stopping power ratio (SPR) training errors for individual tissues by using basis vector method to estimate the relative electron density and applying different ways of predicting I and SPR as discussed above. SPR: Stopping power ratio, BVM: Basis vector method

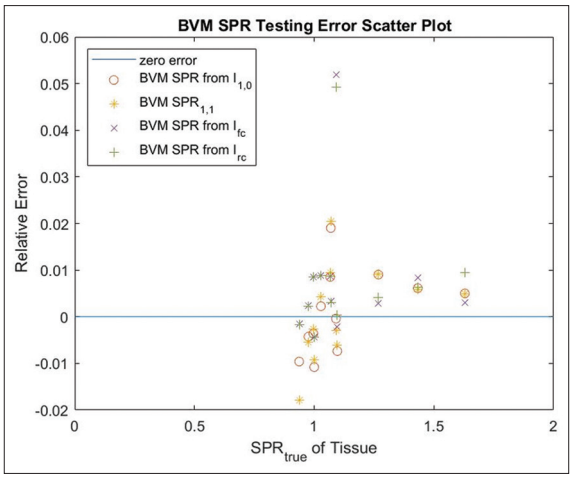

Figure 7: Stopping power ratio (SPR) testing errors for individual tissues by using basis vector method to estimate the relative electron density and applying different ways of predicting I and SPR as discussed above. SPR: Stopping power ratio, BVM: Basis vector method

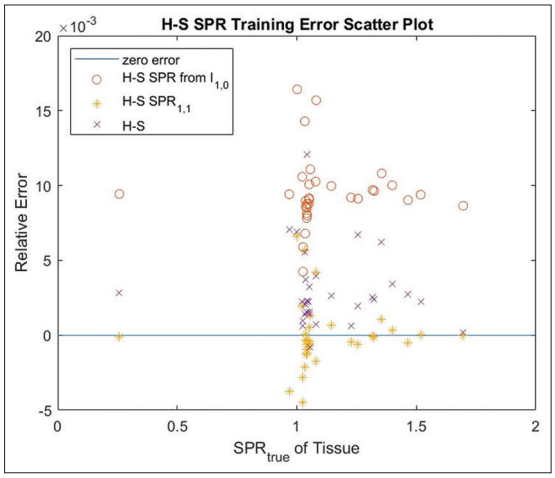

Figure 8: Stopping power ratio (SPR) training errors for individual tissues by using H-S to estimate the relative electron density and applying different ways of predicting I and SPR as discussed above. SPR: Stopping power ratio, H-S: Hunemohr and Saito

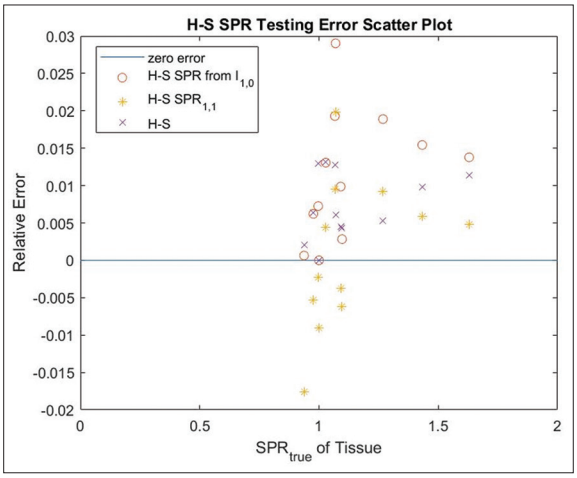

Figure 9: Stopping power ratio (SPR) testing errors for individual tissues by using H-S to estimate the relative electron density and applying different ways of predicting I and SPR as discussed above. SPR: Stopping power ratio, H-S: Hunemohr and Saito

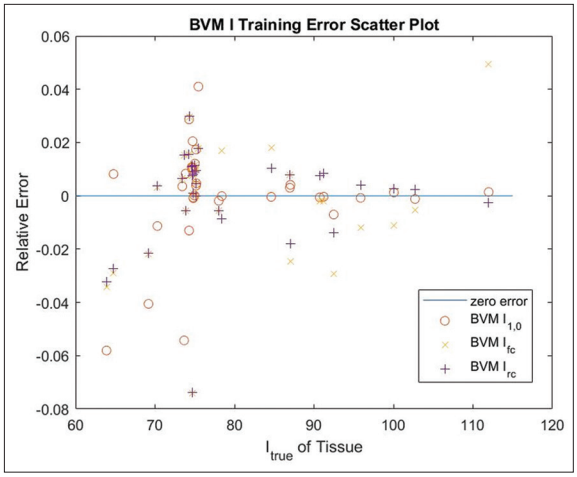

Figure 10: I training errors for individual tissues by using basis vector method to estimate the relative electron density and applying different ways of predicting I as discussed above. BVM: Basis vector method

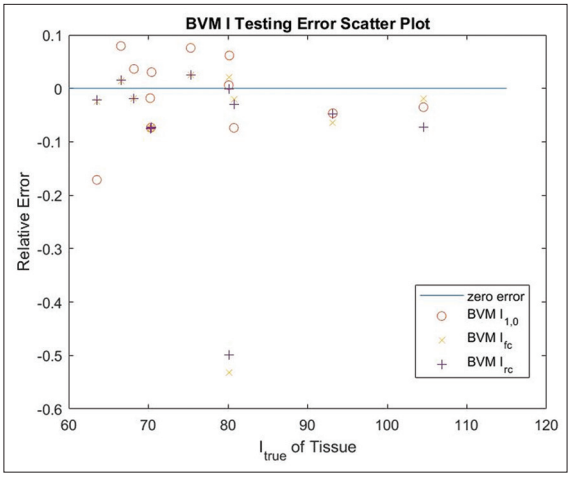

Figure 11: I testing errors for individual tissues by using basis vector method to estimate the relative electron density and applying different ways of predicting I as discussed above

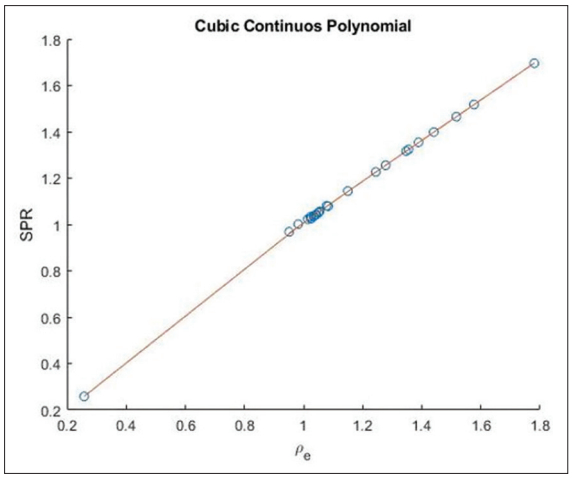

Figure 12: This is the modeling plot of $SPR_{0,3}$ (shows the relationship between the actual stopping power ratio data and the proposed model). SPR: Stopping power ratio

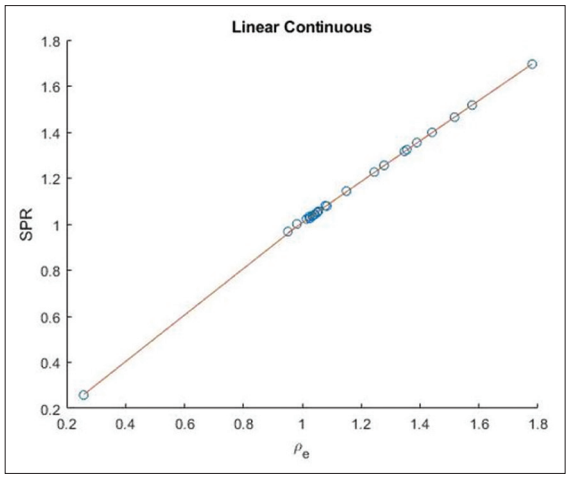

Figure 13: This is the modeling plot of $SPR_{1,1}$ continuous (shows the relationship between the actual stopping power ratio data and the fitted model). SPR: Stopping power ratio

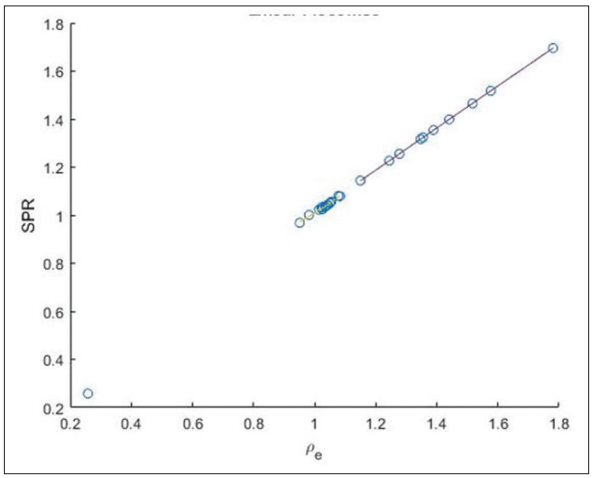

Figure 14: This is the modeling plot of $SPR_{1,1}$ piece-wise (shows the relationship between the actual stopping power ratio data and the proposed model). SPR: Stopping power ratio

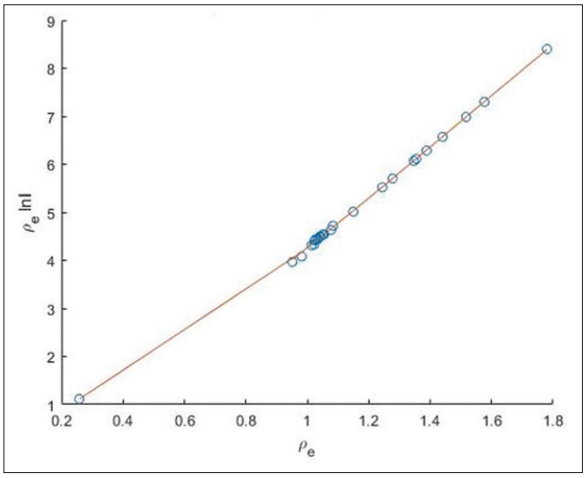

Figure 15: This is the modeling plot of $\rho_e I_{1,2}$ (shows the relationship between the actual data and the fitted model)

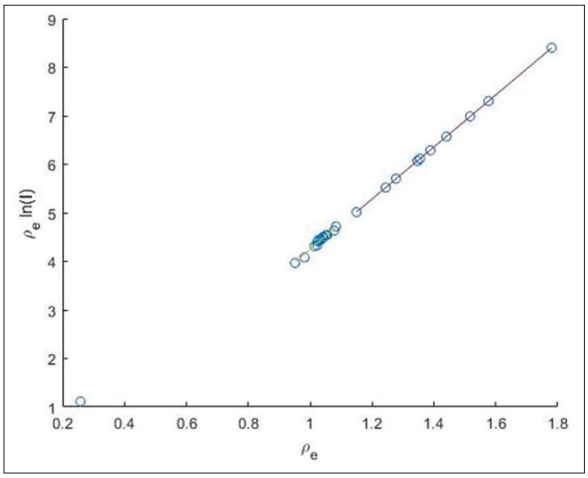

Figure 16: This is the modeling plot of $\rho_e I_{1,0}$ (shows the relationship between the actual data and the fitted model)

Table 8: *I* training and testing root mean square error (%)

I training RMSE	Total	Lung	Soft	Bone	Testing RMSE	Total	Soft	Bone
BVM $I_{1,0}$	1.92	0.39	2.40	0.27		7.19	8.40	5.04
BVM I_{fc}	2.16	0.00	2.23	2.11		15.97	5.12	23.99
BVM I_{rc}	1.84	0.00	2.20	0.92		15.15	5.11	22.68
H-S $I_{1,0}$	1.94	0.00	2.42	0.27		7.21	8.43	5.03
H-S	1.95	0.00	2.23	1.41		4.71	5.13	4.05

BVM: Basis vector method, H-S: Hunemohr and Saito, RMSE: Root mean square error

We can write an application algorithm as follows:

- Given ρ_e data
- Formulate models
- Try different combination of r and n for the proposed model

Table 9: *I* training and testing mean error (%)

I training ME	Total	Lung	Soft	Bone	Testing ME	Total	Soft	Bone
BVM $I_{1,0}$	−0.01	0.39	−0.02	−0.01		−1.08	−0.59	−1.76
BVM I_{fc}	−0.01	0.00	−0.05	0.05		−7.02	−3.25	−12.30
BVM I_{rc}	−0.01	0.00	−0.02	0.00		−7.28	−3.18	−13.02
H-S $I_{1,0}$	−0.02	0.00	−0.03	0.00		−1.09	−0.59	−1.78
H-S	−0.04	0.00	−0.06	0.00		−3.14	−3.26	−2.97

BVM: Basis vector method, H-S: Hunemohr and Saito, ME: Mean error

- Check their training and testing error
- Choose the optimal model for your data.

Conclusion

The presented method gave training RMSE of ≤0.32% and RMSE of ≤0.92% for testing with training ME of 0.02% for SPR. Mean excitation energy *I* has a training error of ≤2.63% and 0.11% for ME. A similar level of accuracy is achieved in application, especially in BVM case. The proposed method proved to be more robust as it performed better on testing data in most cases. It is also more flexible and easy to use as it can give a good result without grouping the tissues, i.e., you can get a good result with continuous model.

The presented machine learning algorithm allows us to adapt the model to different ρ_e data as well as improve its accuracy. It shows that we can improve the accuracy using tissue classification/grouping, increasing/reducing the model degree, and improvement in training data used. This method gives a highly accurate estimation of SPR and *I* as well as giving room for improvement and flexibility. The result will help to provide an accurate proton range value that will enhance more robust treatment planning for proton therapy treatments. Hence, we will carry out more detailed theoretical and empirical analysis on improving and implementing this method in our future work.

Acknowledgments

I would like to acknowledge Dr. Ming Yang for his mentorship on introducing me to proton therapy research and Dr. Hugh Lee for his assistant, especially with some data. My appreciation goes to the University of Texas at MD Anderson Cancer Center for providing me with their facilities at some point of this research.

Financial support and sponsorship

Nil

Conflicts of interest

There are no conflicts of interest.

References

1. Lee HH, Park YK, Duan X, Jia X, Jiang S, Yang M. Convolutional neural network based proton stopping-power-ratio estimation with dual-energy CT: A feasibility study. Phys Med Biol 2020;65:215016.
2. Chika CE, Hooshyar MA. An electromagnetic inverse scattering problem for dielectrics that depend on two spatial variables via eikonal approximation. Microw Opt Technol Lett 2019;61:1517-23. [doi: 10.1002/ mop.31752].
3. Lee HH, Li B, Duan X, Zhou L, Jia X, Yang M. Systematic analysis of the impact of imaging noise on dual-energy CT-based proton stopping power ratio estimation. Med Phys 2019;46:2251-63.
4. Zhang S, Han D, Williamson JF, Zhao T, Politte DG, Whiting BR, *et al.* Experimental implementation of a joint statistical image reconstruction method for proton stopping power mapping from dual-energy CT data. Med Phys 2019;46:273-85.
5. Zhang S, Han D, Politte DG, Williamson JF, O'Sullivan JA. Impact of joint statistical dual-energy CT reconstruction of proton stopping power images: Comparison to image- and sinogram-domain material decomposition approaches. Med Phys 2018;45:2129-42.
6. Shen C, Li B, Lou Y, Yang M, Zhou L, Jia X. Multienergy element-resolved cone beam CT (MEER-CBCT) realized on a conventional CBCT platform. Med Phys 2018;45:4461-70.
7. Yang M, Virshup G, Clayton J, Zhu XR, Mohan R, Dong L. Theoretical variance analysis of single- and dual-energy computed tomography methods for calculating proton stopping power ratios of biological tissues. Phys Med Biol 2010;55:1343-62.
8. Yang M, Zhu XR, Park PC, Titt U, Mohan R, Virshup G, *et al.* Comprehensive analysis of proton range uncertainties related to patient stopping-power-ratio estimation using the stoichiometric calibration. Phys Med Biol 2012;57:4095-115.
9. Schneider U, Pedroni E, Lomax A. The calibration of CT hounsfield units for radiotherapy treatment planning. Phys Med Biol 1996;41:111-24.
10. Bär E, Lalonde A, Royle G, Lu HM, Bouchard H. The potential of dual-energy CT to reduce proton beam range uncertainties. Med Phys 2017;44:2332-44.
11. Bazalova M, Carrier JF, Beaulieu L, Verhaegen F. Dual-energy CT-based material extraction for tissue segmentation in Monte Carlo dose calculations. Phys Med Biol 2008;53:2439-56.
12. Saito M. Potential of dual-energy subtraction for converting CT numbers to electron density based on a single linear relationship. Med Phys 2012;39:2021-30.
13. Landry G, Seco J, Gaudreault M, Verhaegen F. Deriving effective atomic numbers from DECT based on a parameterization of the ratio of high and low linear attenuation coefficients. Phys Med Biol 2013;58:6851-66.
14. Hünemohr N, Krauss B, Tremmel C, Ackermann B, Jäkel O, Greilich S. Experimental verification of ion stopping power prediction from dual energy CT data in tissue surrogates. Phys Med Biol 2014;59:83-96.
15. Hünemohr N, Paganetti H, Greilich S, Jäkel O, Seco J. Tissue decomposition from dual energy CT data for MC based dose calculation in particle therapy. Med Phys 2014;41:061714.
16. Bourque AE, Carrier JF, Bouchard H. A stoichiometric calibration method for dual energy computed tomography. Phys Med Biol 2014;59:2059-88.
17. Garcia LI, Azorin JF, Almansa JF. A new method to measure electron density and effective atomic number using dual-energy CT images. Phys Med Biol 2016;61:265-79.
18. Lalonde A, Bouchard H. A general method to derive tissue parameters for Monte Carlo dose calculation with multi-energy CT. Phys Med Biol 2016;61:8044-69.
19. Farace P. Experimental verification of ion stopping power prediction from dual energy CT data in tissue surrogates. Phys Med Biol 2014;59:7081-4.
20. Taasti VT, Petersen JB, Muren LP, Thygesen J, Hansen DC. A robust empirical parametrization of proton stopping power using dual energy CT. Med Phys 2016;43:5547.
21. Saito M, Sagara S. Simplified derivation of stopping power ratio in the human body from dual-energy CT data. Med Phys 2017;44:4179-87.
22. Li B, Lee HC, Duan X, Shen C, Zhou L, Jia X, *et al.* Comprehensive analysis of proton range uncertainties related to stopping-power-ratio estimation using dual-energy CT imaging. Phys Med Biol 2017;62:7056-74.
23. Saito M, Tsukihara M. Technical note: Exploring the limit for the conversion of energy-subtracted CT number to electron density for high-atomic-number materials. Med Phys 2014;41:071701.
24. Alvarez RE, Macovski A. Energy-selective reconstructions in X-ray computerized tomography. Phys Med Biol 1976;21:733-44.
25. Lehmann LA, Alvarez RE, Macovski A, Brody WR, Pelc NJ, Riederer SJ, *et al.* Generalized image combinations in dual KVP digital

radiography. Med Phys 1981;8:659-67.
26. Chuang KS, Huang H. Comparison of four dual energy image decomposition methods. Phys Med Biol 1988;33:455-66.
27. Schlomka JP, Roessl E, Dorscheid R, Dill S, Martens G, Istel T, *et al*. Experimental feasibility of multi-energy photon-counting K-edge imaging in pre-clinical computed tomography. Phys Med Biol 2008;53:4031-47.
28. Han D, Siebers JV, Williamson JF. A linear, separable two-parameter model for dual energy CT imaging of proton stopping power computation. Med Phys 2016;43:600.
29. Han D, Porras-Chaverri MA, O'Sullivan JA, Politte DG, Williamson JF. Technical note: On the accuracy of parametric two-parameter photon cross-section models in dual-energy CT applications. Med Phys 2017;44:2438-46.
30. Bethe H. Zur theorie des durchgangs schneller korpuskularstrahlen durch materie. Ann Phys 1930;397:325-400.
31. Williamson JF, Li S, Devic S, Whiting BR, Lerma FA. On two-parameter models of photon cross sections: Application to dual-energy CT imaging. Med Phys 2006;33:4115-29.
32. Herman GT, Trivedi SS. A comparative study of two postreconstruction beam hardening correction methods. IEEE Trans Med Imaging 1983;2:128-35.
33. Herman GT. Correction for beam hardening in computed tomography. Phys Med Biol 1979;24:81-106.
34. Evans JD, Whiting BR, Politte DG, O'Sullivan JA, Klahr PF, Williamson JF. Experimental implementation of a polyenergetic statistical reconstruction algorithm for a commercial fan-beam CT scanner. Phys Med 2013;29:500-12.
35. Whiting BR. Signal statistics in X-ray computed tomography. Proc SPIE 4682 Med Imag 2002;4682:53-60.
36. Lasio GM, Whiting BR, Williamson JF. Statistical reconstruction for x-ray computed tomography using energy-integrating detectors. Phys Med Biol 2007;52:2247-66.
37. Csisaar I. Why least squares and maximum entropy? An axiomatic approach to inference for linear inverse problems. Ann Stat 1991;19:2032-66.
38. Williamson JF, Whiting BR, Benac J, Murphy RJ, Blaine GJ, O'Sullivan JA, *et al*. Prospects for quantitative computed tomography imaging in the presence of foreign metal bodies using statistical image reconstruction. Med Phys 2002;29:2404-18.
39. Evans JD, Politte DG, Whiting BR, O'Sullivan JA, Williamson JF. Noise-resolution tradeoffs in X-ray CT imaging: A comparison of penalized alternating minimization and filtered backprojection algorithms. Med Phys 2011;38:1444-58.
40. Yang M, Virshup G, Clayton J, Zhu XR, Mohan R, Dong L. Does kV-MV dual-energy computed tomography have an advantage in determining proton stopping power ratios in patients? Phys Med Biol 2011;56:4499-515.
41. Kanematsu N, Matsufuji N, Kohno R, Minohara S, Kanai T. A CT calibration method based on the polybinary tissue model for radiotherapy treatment planning. Phys Med Biol 2003;48:1053-64.
42. Berger MJ, Hubbell JH, Seltzer SM, Chang J, Coursey JS, Sukumar R, *et al*. XCOM: Photon Cross Section Database. Ver.1.3. 2005.
43. Flohr TG, McCollough CH, Bruder H, Petersilka M, Gruber K, Süss C, *et al.* First performance evaluation of a dual-source CT (DSCT) system. Eur Radiol 2006;16:256-68.
44. Chen Y, O'Sullivan JA, Politte DG, Evans JD, Han D, Whiting BR, *et al.* Line integral alternating minimization algorithm for dual-energy X-ray CT image reconstruction. IEEE Trans Med Imaging 2016;35:685-98.
45. Zhang S, Han D, Politte D, Porras-Chaverri M, Whiting B, Williamson J, *et al*. Basis vector model based method for proton stopping power estimation from experimental dual energy CT data. Med Phys 2016;43:3756.
46. Zhang S, Han D, Politte DG, Williamson JF, O'Sullivan JA. Comparison of integrated and post-reconstruction dual-energy ct proton stop- ping power ratio estimation approaches. Med Phys 2017;44:3004.
47. Stevenson R, Delp E. Fitting Curves with Discontinuities. In: Proc. The First International Workshop on Robust Computer Vision; 1990. p. 127-36.
48. Degirmenci S, Politte DG, Bosch C, Tricha N, O'Sullivan JA. Acceleration of iterative image reconstruction for X-ray imaging for security applications. Proc SPIE Comput Imag 2015;9401:94010C.
49. Zygmanski P, Gall KP, Rabin MS, Rosenthal SJ. The measurement of proton stopping power using proton-cone-beam computed tomography. Phys Med Biol 2000;45:511-28.
50. O'Sullivan JA, Benac J, Williamson JF. Alternating minimization algorithm for dual energy X-ray CT. Proc IEEE Int Symp Biomed Imaging 2004;1:579-82.
51. O'Sullivan JA, Benac J. Alternating minimization algorithms for transmission tomography. IEEE Trans Med Imaging 2007;26:283-97.
52. Paganetti H. Range uncertainties in proton therapy and the role of Monte Carlo simulations. Phys Med Biol 2012;57:R99-117.
53. Park PC, Zhu XR, Lee AK, Sahoo N, Melancon AD, Zhang L, *et al*. A beam-specific planning target volume (PTV) design for proton therapy to account for setup and range uncertainties. Int J Radiat Oncol Biol Phys 2012;82:e329-36.
54. Yang M, Virshup G, Mohan R, Shaw CC, Zhu XR, Dong L. Improving accuracy of electron density measurement in the presence of metallic implants using orthovoltage computed tomography. Med Phys 2008;35:1932-41.
55. Torikoshi M, Tsunoo T, Sasaki M, Endo M, Noda Y, Ohno Y, *et al*. Electron density measurement with dual-energy x-ray CT using synchrotron radiation. Phys Med Biol 2003;48:673-85.
56. Berger MJ, Hubbell JH, Seltzer SM, Chang J, Coursey JS, Sukumar R, *et al*. XCOM: Photon Cross Section Data-Base. Ver. 1.5. Gaithersburg, MD: National Institute of Standards and Technology; 2010.
57. White DR, Woodard HQ, Hammond SM. Average soft-tissue and bone models for use in radiation dosimetry. Br J Radiol 1987;60:907-13.
58. White DR, Widdowson EM, Woodard HQ, Dickerson JW. The composition of body tissues (II). Fetus to young adult. Br J Radiol 1991;64:149-59.
59. Woodard HQ. The composition of human cortical bone: Effect of age and of some abnormalities. Clin Orthop Relat Res 1964;37:187-93.
60. Woodard HQ, White DR. The composition of body tissues. Br J Radiol 1986;59:1209-18.
61. Birch R, Marshall M. Computation of bremsstrahlung X-ray spectra and comparison with spectra measured with a Ge(Li) detector. Phys Med Biol 1979;24:505-17.
62. Poludniowski G, Landry G, DeBlois F, Evans PM, Verhaegen F. SpekCalc: A program to calculate photon spectra from tungsten anode x-ray tubes. Phys Med Biol 2009;54:N433-8.
63. ICRU. Tissue Substitutes in Radiation Dosimetry and Measurement. Bethesda, MD: ICRU; 1989.
64. ICRU. Stopping Powers for Electrons and Positrons. Bethesda, MD: ICRU; 1984.
65. ICRU. Stopping Power and Ranges for Protons and Alpha Particles. Bethesda, MD: ICRU; 1993.
66. Kanematsu N, Inaniwa T, Koba Y. Relationship between electron density and effective densities of body tissues for stopping, scattering, and nuclear interactions of proton and ion beams. Med Phys 2012;39:1016-20.

Appendix

33 ICRU tissues used:

Lung(Inflated), Yellow marrow, Adipose, Breast, Red marrow, Eye lens, Skin, Pancreas, GI tract, Testis, Lymph, Kidney, Ovary, Muscles, Brain, Liver, Spleen, Lung(Deflated), Heart (blood filled), Blood, Cartilage, Thyroid, Spongiosa, Sacrum, Vertebral (D6, L3), Femur, Ribs (2^{nd}, 6^{th}), Vertebral C4, Humerus, Ribs (10^{th}), Cranium, Mandible, Cortical bone.

Gammex inserts used:

Adipose (Gammex), Breast (Gammex), True water (Gammex), Solid water (Gammex), Muscle (Gammex), Brain (Gammex), Liver (Gammex), Inner bone (Gammex), B200 (Gammex), CB30 (Gammex), CB50 (Gammex), Cortical bone (Gammex).